Erosion-Corrosion Behavior and Failure Analysis of Offshore Steel Tubular Joint

E. Mahdi[*], A. Rauf, S. Ghani, A. El-Noamany and A. Pakari

Mechanical and Industrial Engineering Department, College of Engineering, Qatar University, P. O. Box 2713, Doha, Qatar, Tel. No: +9744034309,
[*]E-mail: elsadigms@qu.edu.qa

An extensive investigation into the erosion-corrosion behavior and failure analysis of an offshore steel tubular joint has been carried out by using various electrochemical techniques, visual inspection, optical microscope examination, mechanical testing, microstructure examination, chemical analyses, Scanning Electron Microscope (SEM) examination, Finite Element Analysis (FEA) and Computational Fluid Dynamics (CFD). The open circuit potential (OCP) was recorded for the T-joint material in 0.6 M NaCl without and with electrolyte erosion. Potentiodynamic polarization scans were used to study and compare the material resistance against synergistic impact of erosion-corrosion and corrosion. An optical microscope was used to compare the morphology of pitting corrosion in the absence and presence of erosion. The change in the pitting potential due to electrolyte impingement has been discussed. Pits are slightly stretched in the direction of erosion because of the impingement and disruption of the passive layer in that direction.Visual inspection results showed that the T-joint is heavily eroded and corrosion products were noted. Hardness variation was noted along one of the inspected directions which indicated non-uniform heat treatment. Accordingly, a slow cooling process during heat treatment or manufacturing process is believed to have occurred based on the fine grains observed. Tensile test and microstructure examination indicated that the material of the T-joint is low carbon steel. Furthermore, the chemical analysis indicated that the material of the T-joint is AISI 1026. The results of the chemical analysis of the corrosion products indicated a sulfur-dominant type of corrosion attack. SEM examination revealed presence of cracks, aluminum and calcium inclusions and sea water is believed to be the working fluid. CFD simulation indicated that the fast flow issuing from the main small inlet created relatively high turbulent flow at the area where erosion took place. The fatigue cracks initiation and growth is linked to turbulence intensity and pressure fluctuations.

1. INTRODUCTION

Carbon steel pipelines [1] are commonly used to transport oil and gas universally. In chemical industries and many engineering applications, most of the materials confront erosion-corrosion [2] damage because of solid particles present in the fluid streams. During fluid erosion in the presence or absence of solid particles, mechanical forces exerted by fluid and/or solid particles deteriorate the material surface whereas electrochemical reactions damage the material properties during corrosion. The synergistic impact [3] of erosion-corrosion is more damaging than the sum of their individual harm. The rate of electrochemical reaction increases due to the damage of passive layer resulting in the repassivation and metallic dissolution [4,5]. The rate of passivation will be higher than the rate of dissolution if the metal is kept within passivation potential range. For passive material in an aqueous environment, the electrochemical phenomena is usually slow but flowing stream with or without solid particles can damage the passive layer [6,7] depending on the velocity, impingement angle, mechanical properties and shape of particles.

In oil and gas production systems, pipeline defects such as corrosion, dents, gouges, pits, and cracks are increasingly a significant problem. A pipe joint is the connection of pipes that ensures tight sealing and strength [8]. In some cases, pipe joints provide rapid assembly and disassembly or a change in the direction of the pipeline [9]. The most common types used for general-purpose metal pipes are welded, flanged, threaded, bell-and-spigot joints [10]. Pipe joints are essential components in pipelines. Therefore, great attention has been given to their design and failure analysis. Surface cracks are the most common flaws in offshore structure components, especially in welded tubular joints [11,12]. The calculation of stress intensity factors for surface cracks in tubular joints is very important in fatigue life prediction, fracture assessment, and stress corrosion cracking analysis of those components [13–16]. The modeling techniques used in the finite element analysis of tubular joints have been reviewed to obtain information on strength, stress fields and stress intensity factors. A new method for the calculation of stress intensity factors for surface cracks in pipe–plate and tubular joints is developed by Wang and Lambert [17]. It is based on a model of T-plate weld joints with built-in ends and, therefore, accommodates load shedding effects directly. In this paper, a T-joint was submitted for a failure analysis. The actual placement, loading condition, fluid type, and fluid flow directions were not provided. A leakage from the T-joint was detected. Corrosion products were noted on the inner surface along with a localized material removal in the location of the leakage. Accordingly, an extensive investigation into the failure analysis of offshore steel tubular joint has been carried out using erosion-corrosion behavior, visual inspection, optical microscope examination, mechanical testing, microstructure examination, chemical analyses, SEM examination and finite element analysis and computational fluid dynamics.

## 2. EXPERIMENTAL

2.1. Erosion-corrosion behavior

A piece of the T-joint was cut and embedded in epoxy with exposed area of 0.8 cm^2. The sample surface was ground with silicon carbide (SiC) paper up to 600 grit, washed with liquid soap, water, ethanol (C_2H_5OH) and finally dried in the hot air stream.

The electrochemical cell with three basic electrodes is used to perform the corrosion tests with and without erosion by using a magnetic stirrer. The impingement speed of the electrolyte due to magnetic stirrer can be converted to m/s by using the inner diameter of the cell and revolutions per minute (rpm) of the electrolyte. Magnetic stirrer with 700 revolutions per minute (rpm) stirring speed was used to create erosion in the electrolyte. The reference electrode used in 0.6 M NaCl electrolyte was a saturated calomel electrode (SCE). The corrosion behaviors were investigated by using potentiodynamic polarization scans, open circuit potential (OCP) measurements and electrochemical frequency modulation (EFM) technique. The potential sweep rate of 1 mV/s was used to scan the polarization curves for obtaining the passivation and pitting potential values. The changes in corrosion potential, pitting potential and pitting current were monitored with and without electrolyte erosion in 0.6 M NaCl. A sample period of 0.5 second was used to measure open circuit potential with the help of Gamry potentiostat. An optical microscope was used mainly at 500X magnification to compare the pits size with and without erosion in chloride containing environment.

The perturbation signal of the EFM technique was composed of two since waves having frequencies of 0.2 Hz and 0.5 Hz with amplitude of 20 mV RMS. The measurements were performed by EFM to observe the behaviors of both Causality Factors for detection of pitting corrosion in chloride media with and without erosion. Each test was performed for 1 h by using 4 cycles and a repeat time of 2 minutes.

2.2. Visual inspection

Visual inspection aids in detecting discontinuities such as poor welding, surface defects, corrosion pits, general condition, degradation, blockages and foreign materials [11,12]. The objectives of carrying out a visual inspection are to find defects such as discontinuities, cracks or corrosion that may have caused component failure and to direct the analysis in the most accurate direction. In this manner, the failed component was examined; the component was cut vertically through the leakage location using a metal cutting band saw as shown in Figure 1.

(a)   (b)   (c)
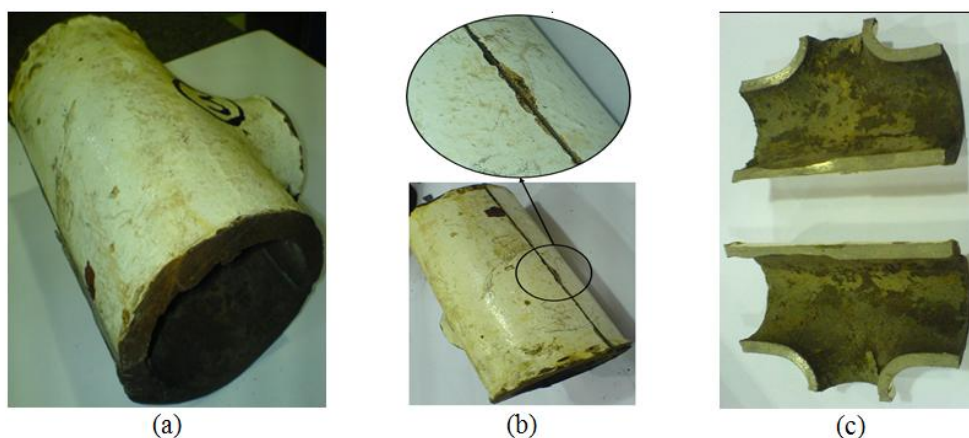
Figure 1. (a) The failed T-joint component (b) The leakage location and a zoomed in view (c) Two halves of tubular Joint

2.3. Optical Microscopy

The objectives of conducting an optical microscope examination on the damaged surface of the T-joint are to identify the condition of the surface and find cracks if present. A part was cut from the location of failure. The part with the location of interest is shown in Figure 2. Note that other specimens are machined to conduct other tests. This part is then cleaned using a plastic brush in a 10% H_2SO_4 solution to remove corrosion deposits.

Figure 2. The part with the location of interest (first from the left)

2.4. Tensile test

The objective of conducting a tensile test on specimens made from the failed component is to obtain the mechanical properties of T-joint material. Based on the dimensions included in the ASTM standard E8/8M-08, the specimens were prepared. The standard specimen shape is shown in Figure 3a.
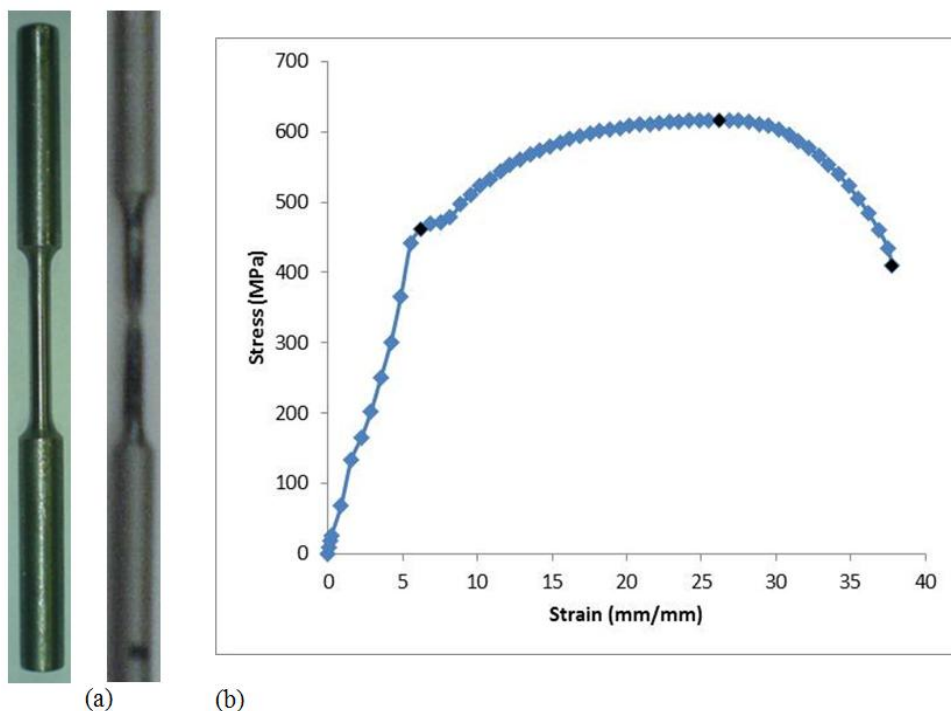
Figure 3. (a) Original and deformed specimens (b) Stress-Strain curve of the T-joint material

Hardness test

A measurement or estimation of the mechanical properties of one or more components involved in a failure is frequently needed as part of the failure analysis. Often, the dimensions of the component(s) limit the use of traditional mechanical testing, and alternative approaches to determine the mechanical properties are required. Micron and sub-micron indentation hardness tests present a viable alternative to traditional testing. Micro and Nano hardness testing provide a smaller length scale, relative to macro-hardness testing, for the evaluation of the hardness for the estimation of other mechanical properties, thus allowing for the testing of even the smallest components. The purpose of performing the hardness test is to check for any variation of hardness in the T-joint. Also, the data produced from the test can be used to verify heat treatment. The equipment used to perform the hardness test is an automated apparatus for making Rockwell and Brinell hardness measurements. The Rockwell hardness scale used was scale B with a 1/16 inch diameter ball indenter.

2.5. Microstructure

Metallography is the study of the microstructure of materials. The microstructure consists of the phases present, grain size, grain boundary, impurities, imperfections, dislocations, etc. The physical and mechanical properties are directly related to the microstructure of a material. Analysis of the microstructure of a material aids in determining if the material has been processed correctly and is, therefore, a critical step for determining product reliability and for determining why a material failed. The basic steps for proper metallographic specimen preparation include: cutting, mounting, rough grinding, fine grinding, polishing and etching. After that, the specimen may be examined by the microscope. The objectives of carrying out a microstructure examination are to obtain an indication of the material of the failed T-joint, to recognize the manufacturing process of the component and its reliability and to gain an indication of the material properties of the material used to make the component.

A specimen with the required size is cut from the T-joint using the abrasive cutting machine. The specimen was mounted using the mounting (pressing) machine. By applying pressure using the handle while keeping the pressure release valve closed, the platform rose; the specimen was then placed in the center of the platform. The pressure release valve was opened to allow the platform to move downward. After that, a specified amount of the phenolic powder was inserted over the specimen and the mold closure was placed. Pressure was applied and the mounting machine was turned on, and the heating process was then started. During heating the pressure was kept at a certain level around 8 MPa. After about 10 minutes the machine was switched off, the heater was removed and the cooler was inserted. The pressure was released using the pressure release valve, the mold closure was removed, pressure was applied again to raise the platform and finally the mounted specimen was removed. The specimen is rough ground using the grinding machine with 120 or 180 particle per inch grade paper. Water is used during this step as a lubricant and a cooler to protect the microstructure from getting damaged. The specimen is fine ground using the roll grinder. The different grinding papers are used one after the other (240, 320, 400 and 600 particles per inch respectively.) The

grinding motion, in each grinding stage, is perpendicular to the scratches from the previous grinding stage. The sample was cleaned thoroughly after this step. The specimen is then polished using Al_2O_3 solutions along with the revolving disk. A mirror-like surface is obtained at the end of the polishing operation. The specimen is etched using Nital (97% ethanol + 3% nitric acid). Nital (which is used as an etchant for iron, steel and cast iron) is used based on the assumption that the material used to make the T-joint is Carbon Steel. The chemical reaction is stopped by immersing the specimen in water for few seconds. The specimen was then dried using hot air.

2.6. Chemical analysis

The objectives of performing chemical analyses are to identify the T-joint material and to find some information about the corrosion process by evaluating the corrosion products inside the T-joint. A specimen with the required size is cut from the T-joint using the abrasive cutting machine. The specimen required some machining to be prepared for performing the chemical analysis. The equipment used to perform the chemical analysis is Optical Emission Spectrometer (OES) for metal analysis (ARL 3460). The chemical analysis was done at 3 locations. The corrosion products (Figure 4) from inside the T-joint were placed inside a container to perform the XRF analysis using the X-Ray Spectrometer JSX-3201M Element Analyzer.

Figure 4. Corrosion products taken from inside the T-joint

2.7. SEM examination

The objectives of conducting a scanning electron microscope (SEM) examination on the T-joint are to identify the condition of the surface, to examine in more details, the cracks in the material, to spot defects in the material if present and to recognize the elements and their relative quantities in one of the examined locations.

3. RESULTS AND DISCUSSION

3.1. Erosion corrosion behavior

3.1.1. Open circuit potential (OCP) measurements

In an electrolyte containing 0.6 M NaCl the OCP was measured by running the test for 30 min to observe the OCP behavior during corrosion at the surface of T-joint metal. The OCP behavior and the surface damage after this test are shown in Figures 5 and 6.
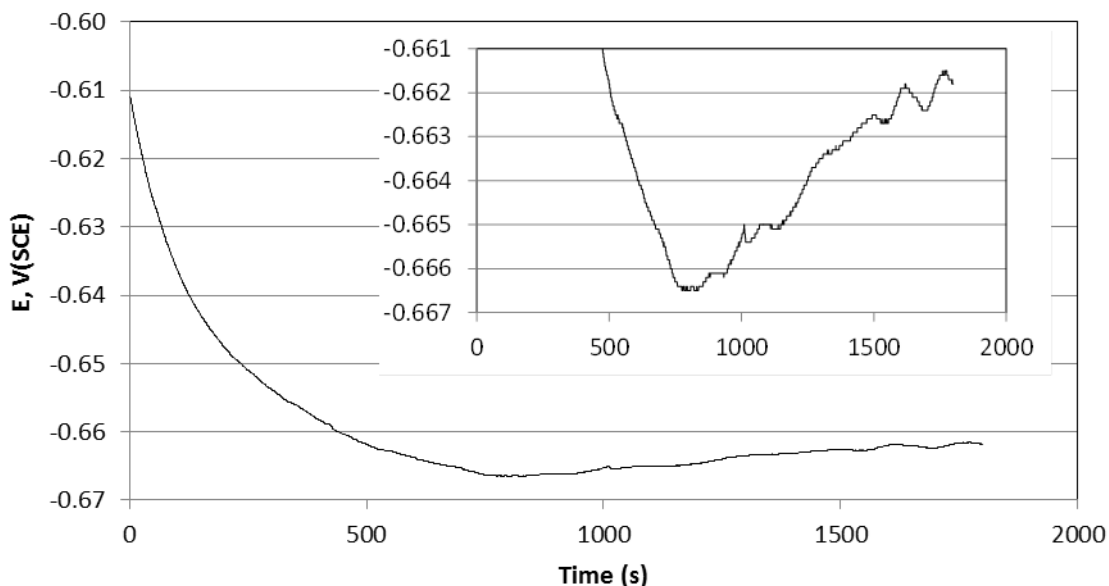

**Figure 5.** The OCP measured for the T-joint material in 0.6 M NaCl. Small pits were observed at the end of the test.
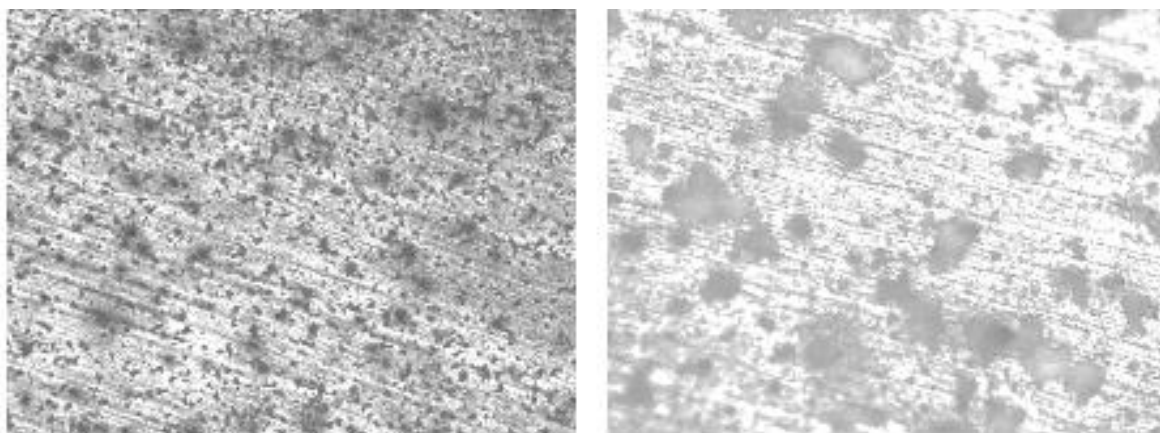
Figure 6. After measuring the OCP for the T-joint material in 0.6 M NaCl, the surface of the metal is shown at 500X and 1000X magnifications.

The OCP (Figure 7) turned noisier with higher fluctuations when tested with electrolyte erosion. Pitting corrosion (Figure 8) was observed after 30 min test with electrolyte erosion.
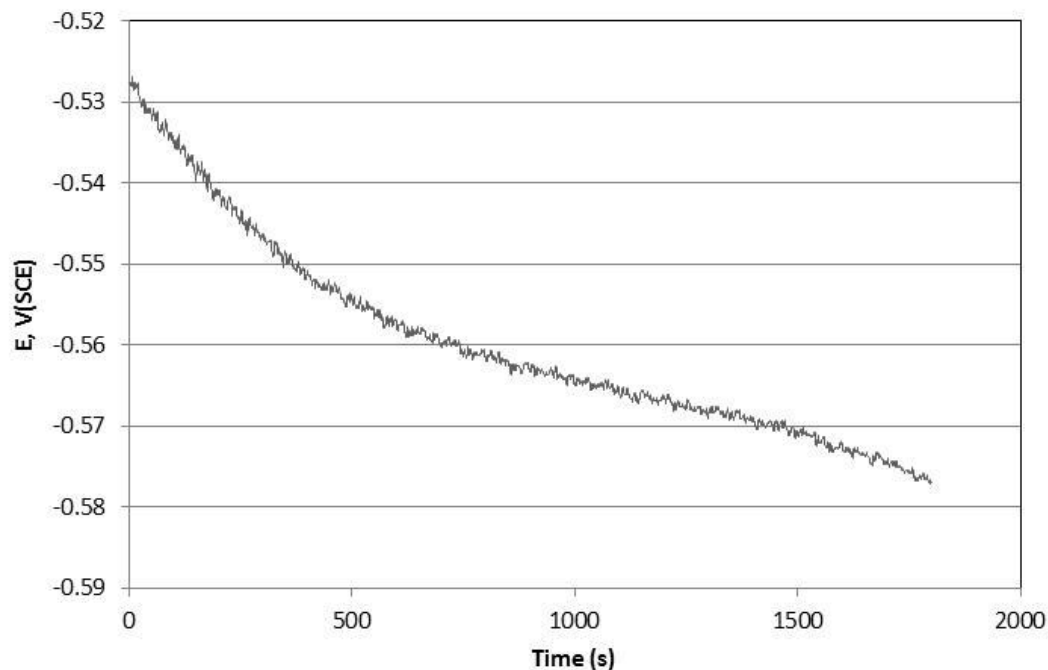
Figure 7. In 0.6 M NaCl, the erosion speed of 3.6 m/s was used to measure the OCP for T-joint sample. Big patches of uniform corrosion and many pits were observed.
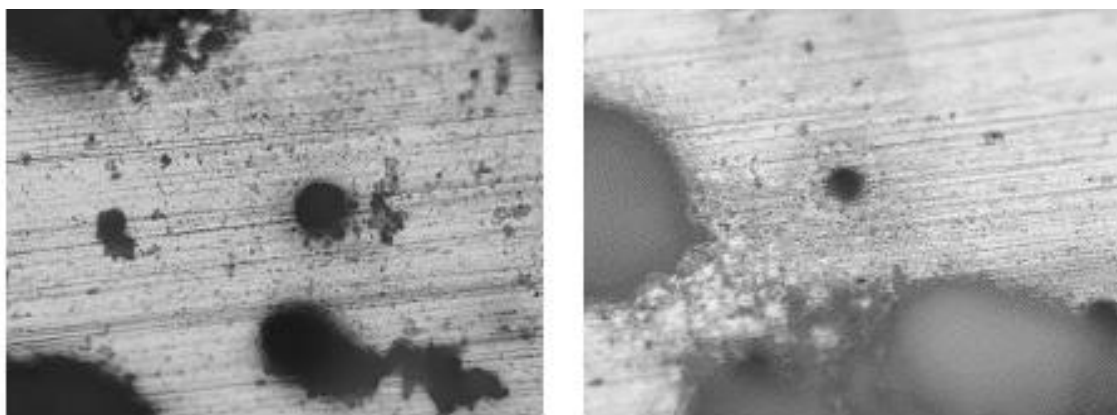
Figure 8. The OCP was measured with fluid erosion for T-joint sample in 0.6 M NaCl. Pits were observed at 500X magnification through optical microscope at various locations of surface of metal.
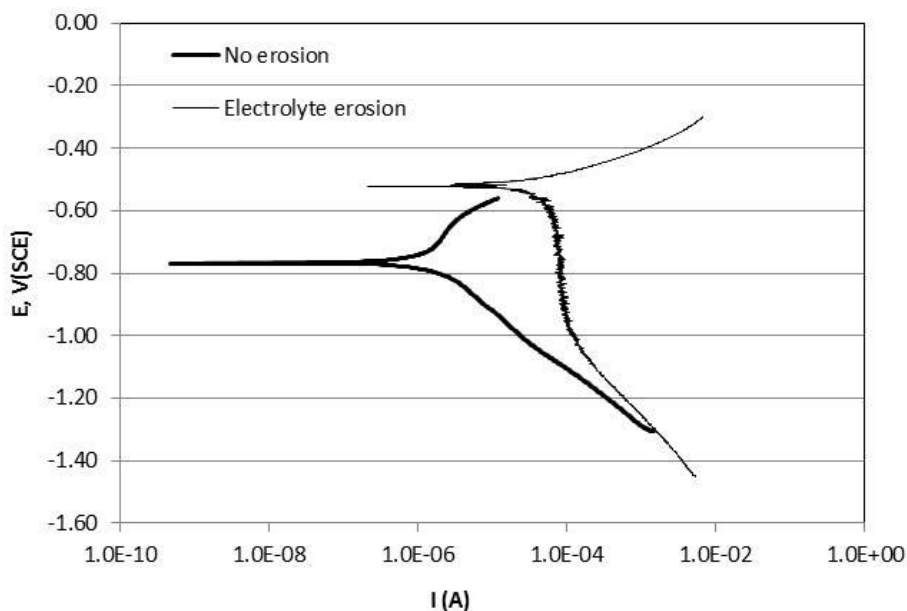
3.1.2. Potentiodynamic polarization scans

During polarization scan (Figure 9) in 0.6 M NaCl, the material sample taken from T-joint demonstrated a reasonable region of passivation. The corrosion and pitting potentials were observed at -768 mV and -630 mV vs. SCE. After finishing the scan, the surface of the metal was observed under optical microscope at 500X magnification and clear pits (Figure 10) were observed.

With electrolyte erosion, many large pits growing in the direction of erosion were observed after potentiodynamic polarization. Corrosion and pitting potentials were nearly at the same potential

(Figure 9) at -500 mV vs. SCE. Due to erosion the size and number of pits (Figure 10) increased as compared to the situation of unstirred electrolyte.

Figure 9. Pitting was observed after potentiodynamic polarization in 0.6 M NaCl without erosion for T-joint material. Corrosion and pitting potentials were found to be -768 mV and -630 mV vs. SCE.
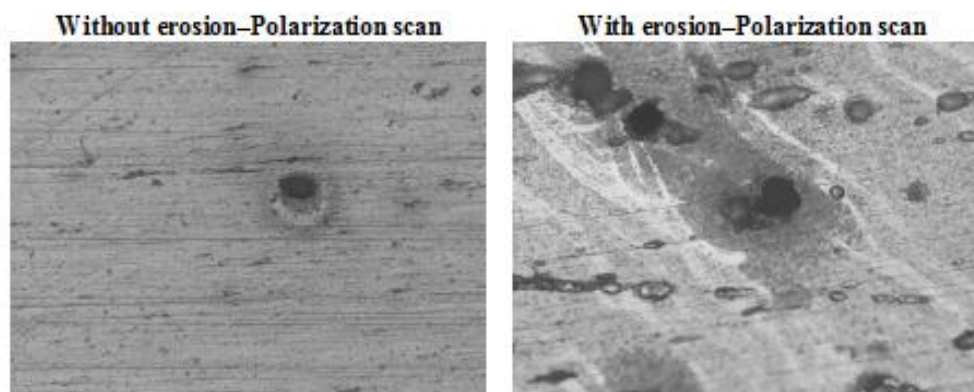

Figure 10. After scanning the potentiodynamic polarization for T-joint sample in 0.6 M NaCl without and with electrolyte erosion. In both cases, pitting corrosion was observed with the help of optical microscope at 500X magnification

3.1.3. EFM measurements

The EFM measurements were performed for 1 h by applying DC potential of -630 mV taken from potentiodynamic polarization scan to observe the occurrence of pitting corrosion and its detection with the help of EFM through its Causality Factors. Causality Factor 3 showed higher values than the normal value of 3 due to pitting corrosion in 0.6 M NaCl whereas Causality Factor 2 remained stable around its normal value of 2 as shown in Figure 11. Causality Factors [18] give higher values and

fluctuate during pitting corrosion. At the end of the experiment pitting corrosion was observed (Figure 13). Again pits were observed by using EFM measurements at pitting potential (-500 mV taken from potentiodynamic polarization) and behavior of Causality Factor 3 (Figure 12) confirmed the detection of pitting corrosion. Bigger pits (Figure 13) were observed due to erosion as compared to unstirred electrolyte.
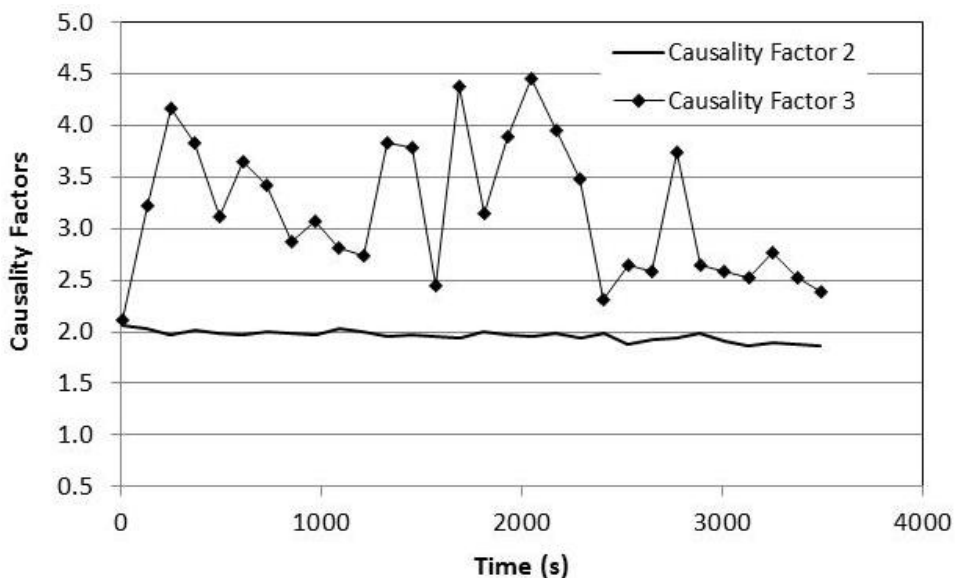
Figure 11. Causality Factors of EFM are fluctuating during pitting corrosion for T-joint sample in 0.6 M NaCl.
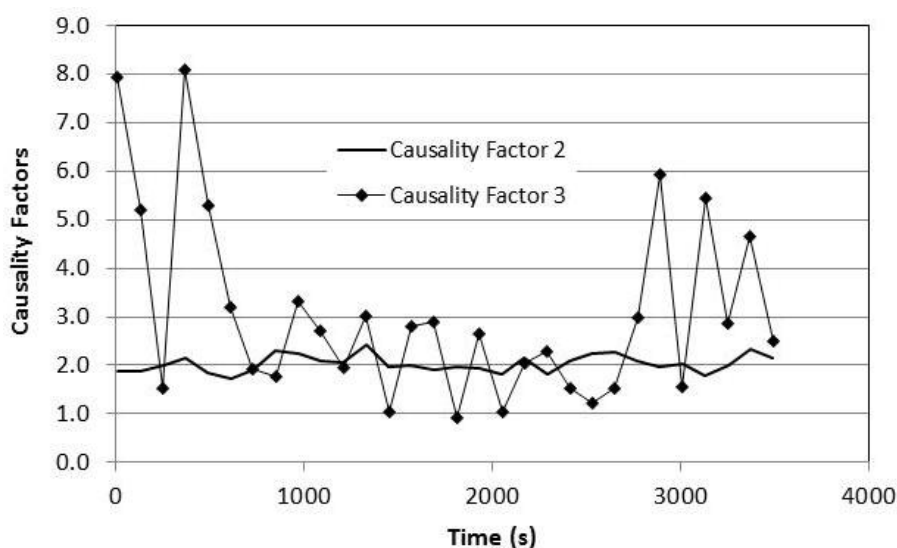
Figure 12. Causality Factors of EFM are fluctuating during pitting corrosion for T-joint sample in 0.6 M NaCl with electrolyte erosion. Many pits growing in the direction of erosion were found. After comparing, the size of pits was found larger than the case of without erosion.
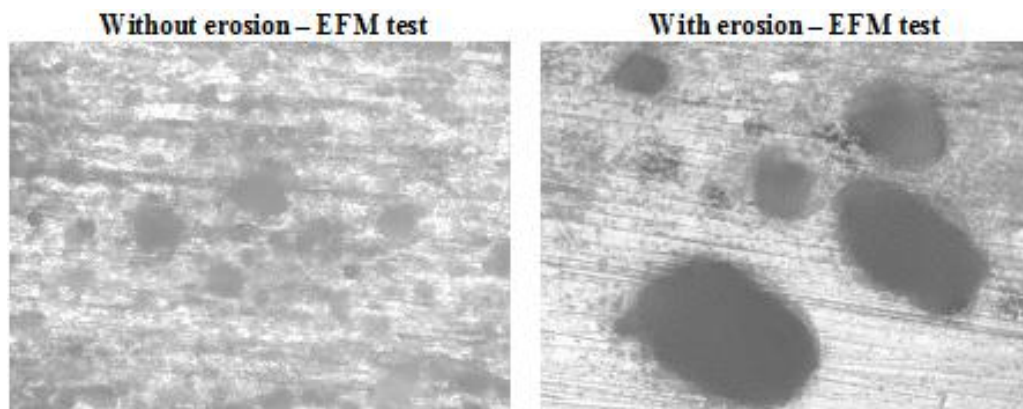
Figure 13. The surface of the sample at 500X magnifications after performing the EFM tests at pitting potentials for 1 h each without and with erosion.

The resistance to pitting corrosion decreases due to erosion in the stirred electrolyte containing chloride content. The passivation becomes negligible due to erosion whereas the pitting potential grows higher due to erosion. The amplitude of OCP fluctuations becomes larger due to erosion-corrosion (Figure 7) with many continuous positive and negative peaks for T-joint metal in chloride containing environment as compared to unstirred electrolyte (Figure 5). After 30 min of the test, many pits were observed (Figure 6) with the help of optical microscope at different magnifications. In case of stirred electrolyte, the size of pits was bigger (Figure 8) than the unstirred electrolyte. The fluctuating OCP has been observed [19,20] due to various types of localized corrosion like pitting, crevice corrosion and stress corrosion cracking for stainless steel in the presence of chloride ions. Pits can repassivate while being metastable and stop growing if the potential is below the pitting potential. Pitting corrosion can start and propagate [6] easily by the increase in potential. The OCP for T-joint sample in stirred electrolyte gave noisier response with higher number of fluctuating peaks suggesting rapid growth and propagation of the pitting corrosion. In case of Al-2.5 Mg alloy in 3% NaCl, the corrosion attack increases due to increased flow rate [21] while the inhibiting efficiency decreases. The induction time [6] is more to reach the stable pitting and the amplitude of the initial spikes is small due to metastable pitting in case of unstirred electrolyte as compared to the stirred electrolyte. Due to larger size and more number of pits, the amplitude of spikes is higher in stirred electrolyte as compared to unstirred electrolyte. In case of unstirred electrolyte the induction time [6] is more to reach stable pitting. Slightly elliptical shaped pits (Figure 8) were observed due to erosion of passive layer in the direction of electrolyte flow. The fall in the OCP is due to the growth of stable pits [6] followed by the large fluctuations because of the propagation of pitting corrosion in a destructive way. The potential fluctuates in positive and negative directions during stable pitting. Severe pitting corrosion was observed after scanning the polarization scans with and without erosion in 0.6 M NaCl. The limiting current density increases and the corrosion potential shifts towards higher potential in stirred electrotype as compared to unstirred solution. In case of cathodic polarization curves, the limiting current density and corrosion potential [22] increase due to high electrode rotational speed for X65 steel in solution containing NaCl and NaHCO$_3$. The high speed of the electrode facilitates the increased rate of the reduction reaction in the electrolyte. Corrosion current, pitting current and pitting

potential become higher due to electrolyte erosion. After polarization scan with electrolyte erosion, bigger and numerous pits were observed as compared to unstirred electrolyte. The shape of the pits after the polarization scan due to erosion was slightly stretched in the direction of erosion whereas the unstirred electrolyte yielded circular pits. The response of EFM with the help of Causality Factors confirms the prediction and occurring of pitting corrosion for T-joint metal in chloride solutions with and without erosion.

3.2. Visual inspection

The leakage location was examined from the inner surface. The component is observed to be painted from the outside with a white colored material as shown in Figures 1a and 1b. Corrosion products are observed on the inner surfaces as shown in Figure 1c. This indicates that the material of the T-joint is susceptible to corrosion; however, the corrosion may have happened during storage. There is a possibility that some corrosion may have happened during service and lead to the failure. The leakage location and a zoomed in view are shown in Figure 1b. A localized removal of material is labeled at the inner walls of the T-joint (see Figure 15a). The direction of the flow can be determined by examining the location of material removal (Figures 14, 15a and 15b). The location of material removal is not directly opposite to inlet 2 but a little to the right as shown in Figure 15a. Figure 15d shows the effect of erosion on the thickness of the T-joint. There is a high possibility that the component was placed with inlet 2 upwards so that gravity accelerates the flow above the normal expected designed velocity; however, this is only true if the gauge pressure inside the pipe sections is close to zero.
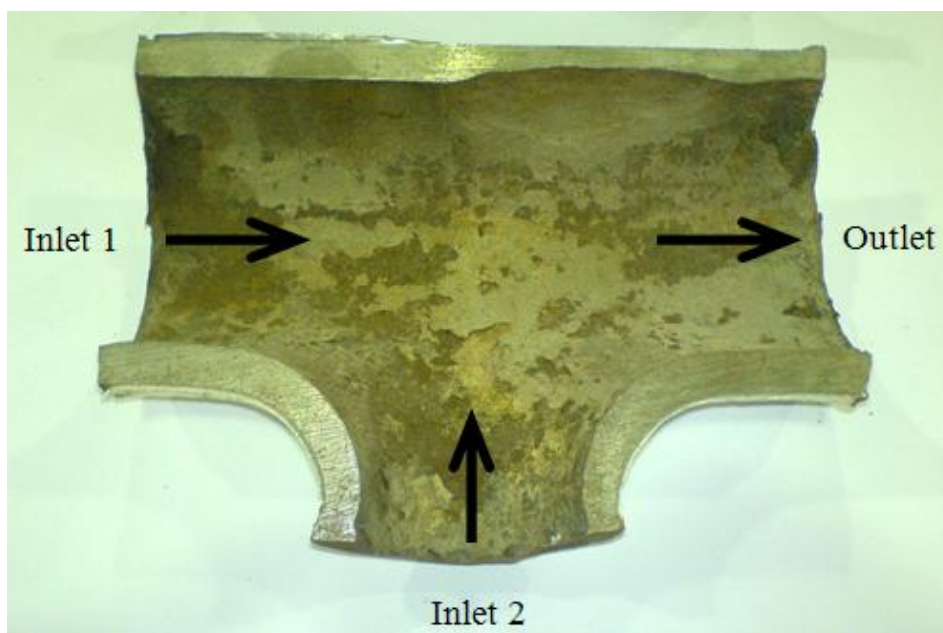
Figure 14. A section showing the flow direction
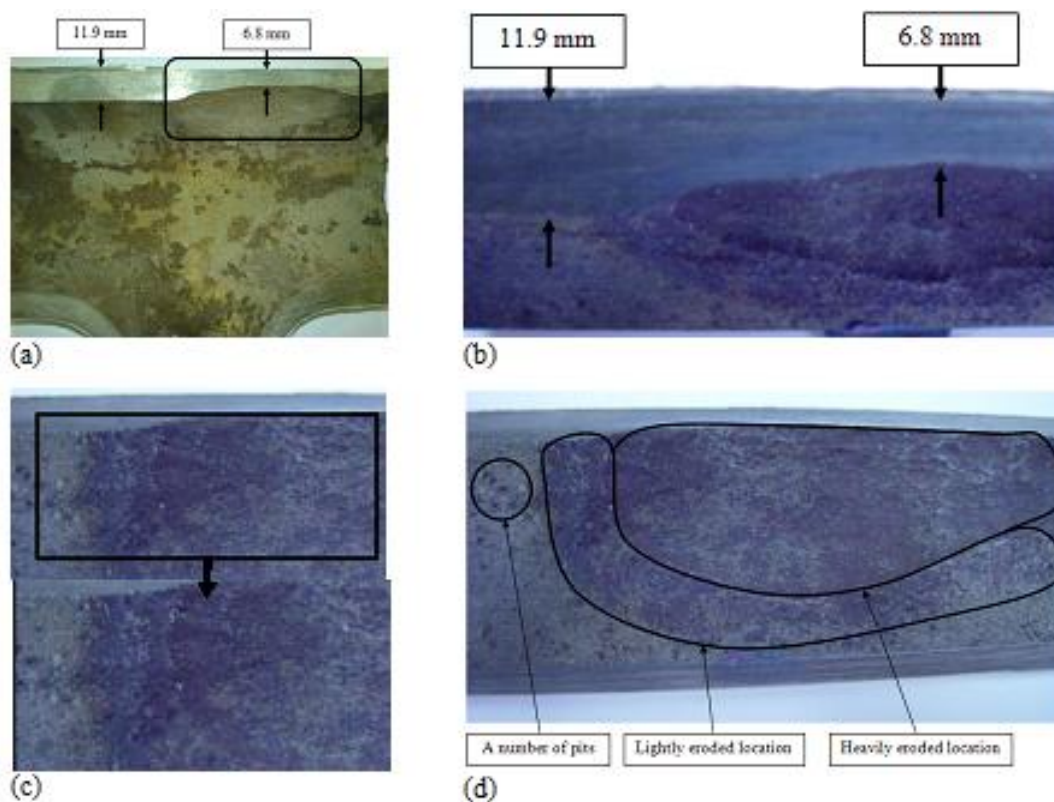
Figure 15. (a) The localized material removal location (b) Magnification of eroded section (c) Eroded section showing a scattered pits location (d) Failure locations.

3.3. Optical microscopy

The cleaned part is examined under the optical microscope. Three locations were identified: a scattered pits location, a lightly eroded location and a heavily eroded location as shown in Figures 15 and 16. Corrosion products were detected on the part. These corrosion products either were not removed while cleaning the part or were a result of the interaction between the newly cleaned surface and surrounding medium (air and moisture).

Figiure 16. Zoomed-in views of the heavily eroded location (magnification increases from left to right)

However, it is noted that erosion was not the only cause of leakage, but fatigue due to the fluctuation of pressure inside the piping system may have initiated a crack similar to the one seen

which caused the leakage when it reached the outer surface. The pits that were noted on the surface may have formed during shutdowns when the working fluid stagnates in the rough eroded surface. These pits may have acted as starting points for cracks which grew due to fatigue and caused the leakage. It is also possible that one of the pits grew till it reached the outer surface of the T-joint and caused the leakage. Erosion, corrosion and fatigue are most likely the three main factors that resulted in the T-joint failure.

3.4. Tensile test

The results about tensile test are presented in Figure 3b. The ultimate tensile strength, fracture strength and the yield strength were calculated to be 628.15 ($\pm$5.73) MPa, 426.02 ($\pm$16.01) MPa and 473.85 ($\pm$5.95) MPa, respectively. Mechanical properties were calculated and given in Table 1 along with the range for these properties obtained from ref. 15. The tested material is proven to be a ductile material since necking was observed, cup and cone fracture surfaces were noted, and because its stress-strain behavior resembles that of ductile materials. The values of the properties calculated for this material lie within the range of the properties of low carbon steels. This verifies the initial guess; however, it is still early to come to a conclusion. To accurately identify the material, the microstructure examination and chemical analysis has been carried out and will be highlighted in next section.

**Table 1.** Mechanical Properties of the T-joint specimen

Specimen Number	Average	Low Carbon Steels
σ_y (MPa)	467.90 ($\pm$5.95)	140 - 2400
σ_{uts} (MPa)	622.43 ($\pm$5.73)	250 - 2450
σ_{fr} (MPa)	426.02 ($\pm$16.01)	3.30 - 1130
%EL	28.75 ($\pm$0.75)	1.00 - 60.0
%RA	69.02 ($\pm$1.82)	15.4 - 75.0

3.5. Hardness test

The hardness test was applied to the specimen in two directions as shown in Figure 17a. The hardness along direction 1 and 2 is presented in Figure 17b. It can be seen that there is almost no variation in hardness along direction 1, while the hardness is higher at the middle of direction 2. Using the average hardness the tensile strength of the T-joint material can be roughly approximated. Using the Standard Hardness Conversion tables the tensile strength is approximated. The average Hardness is 83.5 HRB which is equivalent to 160.5 HB. The relationship between the ultimate tensile strength and the hardness is

TS (MPa) = 3.45 $\times$ HB = 3.45 $\times$ 160.5 = 553.7 MPa

From the tensile test, the strength is approximately 628.15 MPa. The %deviation is approximately 11.85%. From Figure 17b, it can be seen that there is almost no variation of hardness along direction 1, while the hardness is lower near the edges along direction 2 which can indicate that the material is more vulnerable to scratch or indent at the locations where the hardness is lower. Hardness tests across the section cut through the T-joint showed a soft inner zone, followed by a harder zone and then a soft zone which can mean that the outer layers of the T-joint lost carbon due to the heat treatment during manufacture. Also, by performing the hardness test an approximation of the tensile strength of the T-joint material have been found.
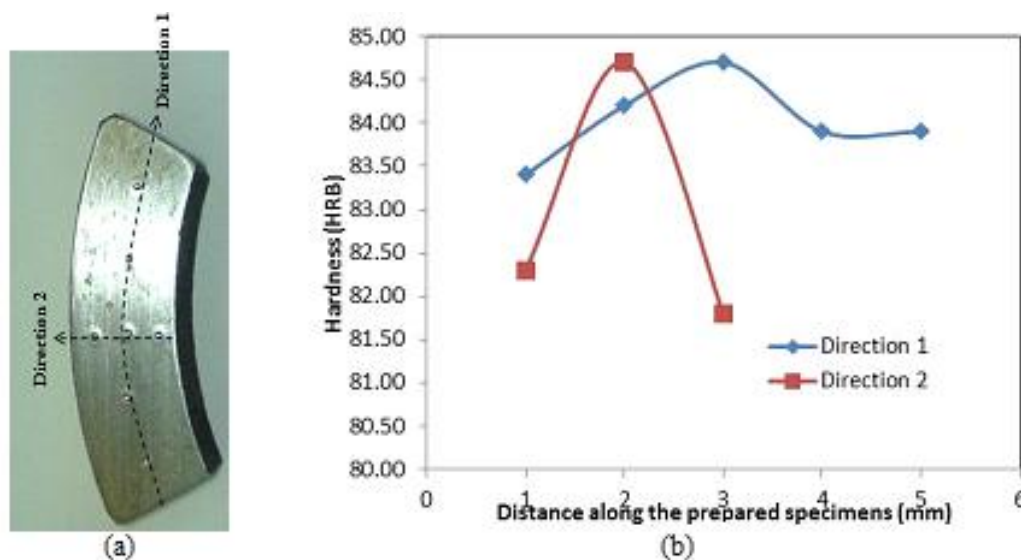
Figure 17. (a) The specimen prepared for hardness test (second from the left) (b) Hardness along directions 1&2 as shown in (a)

3.6. Microstructure

The microstructure at different magnifications (100X, 200X, 500X and 1000X) is shown in Figure 18. The fact that the microstructure was revealed using Nital validates the assumption that the material used to make the T-joint is Carbon Steel. To determine more information concerning this material, the microstructure at a magnification of 1000X is further studied (Figure 19). Two phases can be seen in the microstructure; the light Ferrite and the dark Pearlite phases. The availability of those two phases indicates that the material is Carbon Steel with Carbon content in the range from 0.022 to 0.76 wt% C. The Ferrite phase is a soft and ductile phase, but the Pearlite phase is a hard and brittle phase. The Ferrite phase is available in more quantities than the Pearlite phase. The ratio is approximately 7:3. This indicates that the material is actually Low Carbon Steel (0.05 to 0.25 wt% C). Due to the existence of those two phases, the material properties are expected to be intermediate between them but a little closer to the properties of the Ferrite phase since it is available in more quantities. Also, the metal has likely been slowly cooled during the heat treatment of manufacturing process. ASTM E112 standard test methods considers one of the most widely cited ASTM standards,

is chiefly concerned with the measurement of grain size. Therefore, using ASTM standard E112 [23], the grain size is determined utilizing Figure 21 as follows:

$$M = 1000X$$
$$d_1 = 90mm \Rightarrow L_1 = \pi d_1 = \pi \times 90 = 282.6mm; \ N_1 = 28$$
$$d_2 = 70mm \Rightarrow L_2 = \pi d_2 = \pi \times 70 = 219.8mm; \ N_2 = 19$$
$$d_3 = 50mm \Rightarrow L_3 = \pi d_3 = \pi \times 50 = 157mm; \ N_3 = 15$$
$$L_T = L_1 + L_2 + L_3 = 282.6 + 219.8 + 157 = 659.4mm$$
$$N_T = N_1 + N_2 + N_3 = 28 + 19 + 15 = 62$$
$$P_L = \frac{N_T M}{L_T} = \frac{62 \times 1000}{659.4} = 94.025mm^{-1}$$
$$n = -3.3 + 6.65 \log(P_L) = -3.3 + 6.65 \log(94.025) = 9.8$$

This indicates that the material has small grains. In addition the heat treatment or manufacturing process of the material included a slow cooling process. The material is believed to be soft and ductile rather than hard and brittle; with generally good mechanical properties.
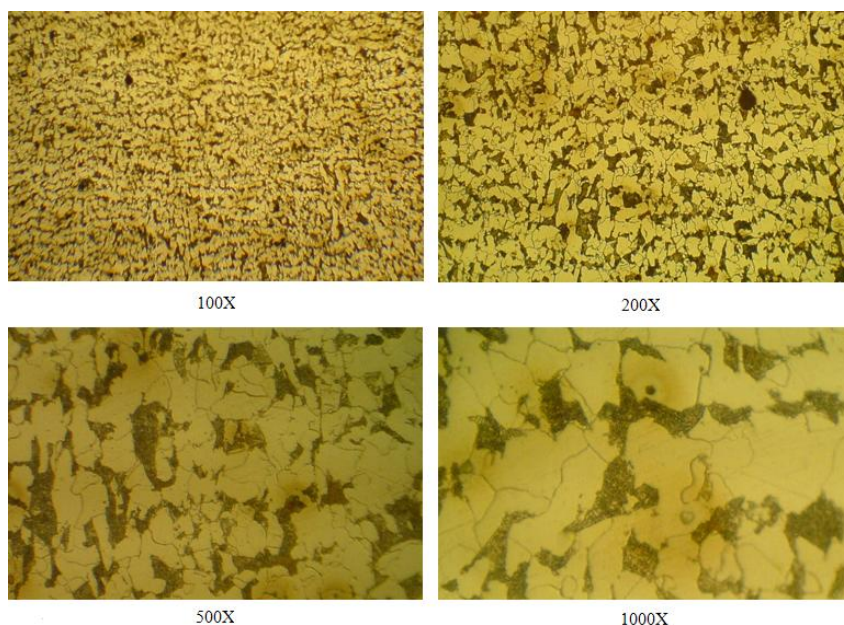
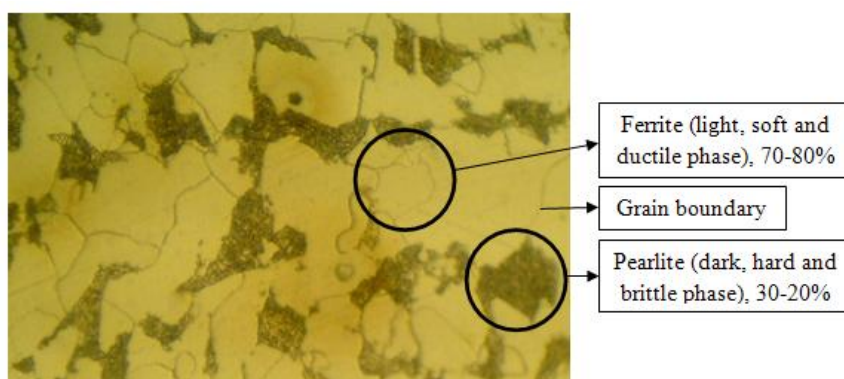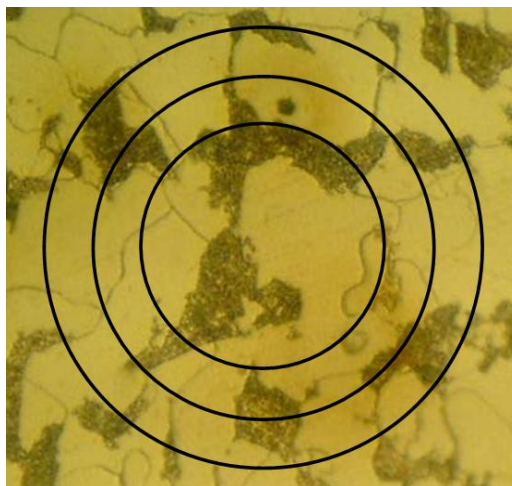**Figure 18.** The microstructure of the T-joint at different magnifications (as indicated)

Figure 19. The microstructure at a magnification of 1000X

Figure 20. Determination of grain size based on ASTM standard E112.

3.7. Chemical analysis

The average of the results from Chemical analysis of the specimen and the possible material of the T-joint are shown in Table 2. It is well-known that steels form one of the most complex group of alloys in common use.

Table 2. Chemical analysis results of the T-joint specimen

Element	Actual % (by weight)	AISI 1026 (%)
SiO_2	42.2323	
P_2O_5	3.1143	0.22 – 0.28
SO_3	1.5653	0.60 – 0.90
K_2O	0.9113	0.040 max
Sulfur (S)	0.03781	0.05 max
Silicon (Si)	0.357403	0.3 – 0.6
Nickel (Ni)	0.087047	Not specified
Chromium (Cr)	0.109753	Not specified
Molybdenum (Mo)	0.02473	Not specified
Copper (Cu)	0.100633	Not specified

The synergistic effect of alloying elements and heat treatment produce a tremendous variety of microstructures and properties (characteristics). It should be noted that the effects of a single alloying elements are modified by the influence of other elements. These interrelations must be considered when evaluating a change in the composition of steel. The chemical composition of the corrosion products was analyzed by means of X-ray fluorescence (XRF) and the results are given in Table 3. Finding iron in large quantity is expected and confirms the corrosion also there is a high sulfur

concentration, which seems to indicate a sulfur-dominant type of corrosion attack. The presence of calcium suggests that the working fluid inside the T-joint might be sea water. Chemical analysis of the T-joint material revealed it to be low carbon steel. Compositions approximately correspond to the AISI 1026 specifications. The results of XRF analysis has been done on the corrosion products inside the T-joint showed a high content of sulfur which indicates a sulfur-dominant type of corrosion attack. Also, sea water was possibly the working fluid causing pitting corrosion.

Table 3. Chemical composition of corrosion products

Element	Mass (%)
Sulfur (S)	15.2927
Calcium (Ca)	12.0741
Iron (Fe)	72.6332

3.8. SEM examination

Using the scanning electron microscope, two of the three parts are scan at five magnifications (100X, 250X, 500X, 1000X and 2000X). The first location is a heavily eroded while the second location is a scattered pits location. At 1000X, the second location is scanned for the elements present and their relative quantities. The SEM images of the two scanned locations at 2000X are shown in Figures 22–26. The Energy-dispersive X-ray spectroscopy (EDS) spectrum was obtained at 1000X magnification. Note both locations are characterized by a rough surface. Some areas are characterized by a white foam or bright appearance. On the first surface, deposits and cracks are noted. On the second surface, cracks and an inclusion are noted. The cracks noted in the heavily eroded location (first location) are longer and are available in larger quantities than in the scattered pits location (second location). The EDS spectrum shows a number of elements that the material of the T-joint is composed of and foreign elements. The foreign materials are Aluminum (Al), Calcium (Ca) and Oxygen (O). The rough surfaces are an indication of erosion. The white foam or bright areas in the images shown above represent corrosion products. The noted cracks indicated that stresses on the T-joint (due to the pressure of the fluid inside) have contributed to the failure. As shown, the cracks are longer and are available in larger quantities in the eroded location which can be explained by noting the thinning that has occurred due to erosion. Note that the rough surface helped to some extent in trapping the cracks and stopping crack growth; however, with repeated loading, the crack eventually reached the surface and caused the leakage which was reported. The foreign elements may represent the inclusions, deposits (that may have come from the working fluid inside the T-joint) or corrosion products. Aluminum is believed to have been identified when scanning the inclusions. On the other hand, Calcium is believed to have been identified when scanning the deposits. Oxygen is believed to have been identified when scanning corrosion products. The working fluid inside the T-joint is probably sea water as Calcium was found in the form of what is believed to be deposits on the inner surface of the T-joint.
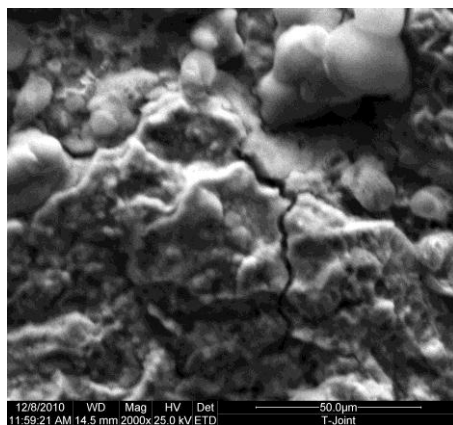
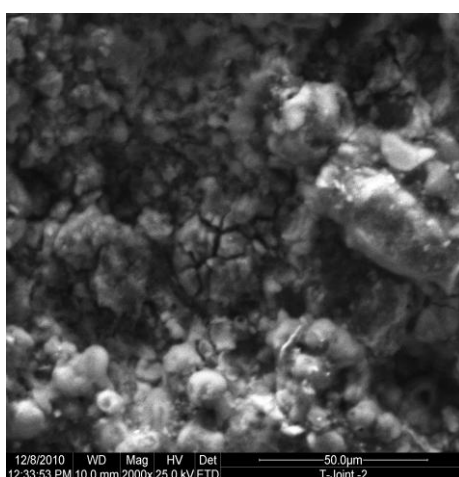**Figure 22**. The SEM image of the first location at 2000X

Figure 23. The SEM image of the second location at 2000X
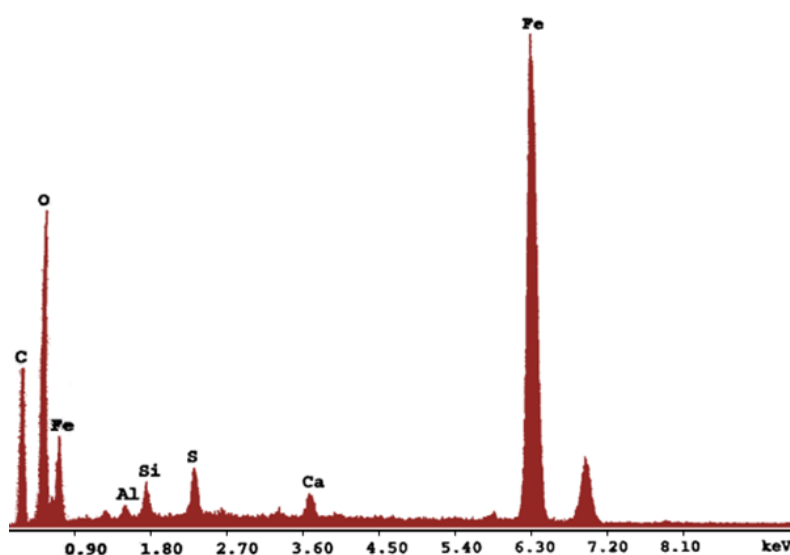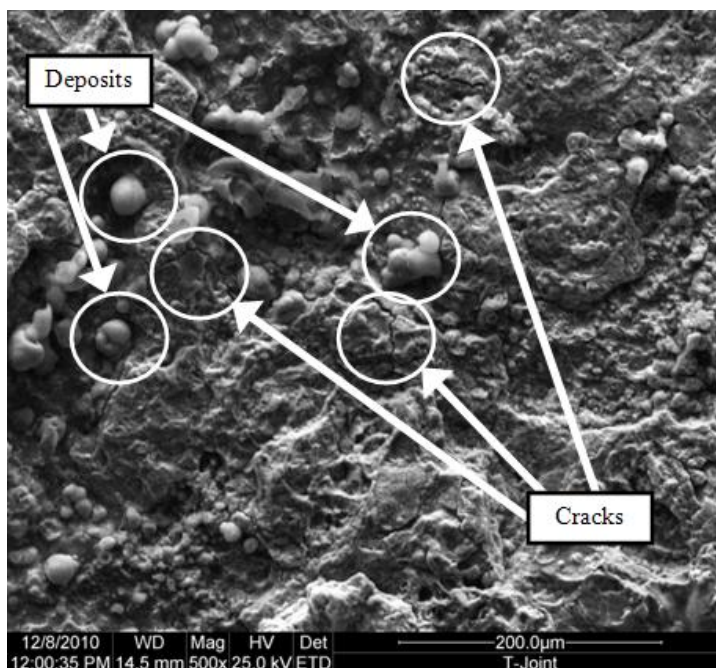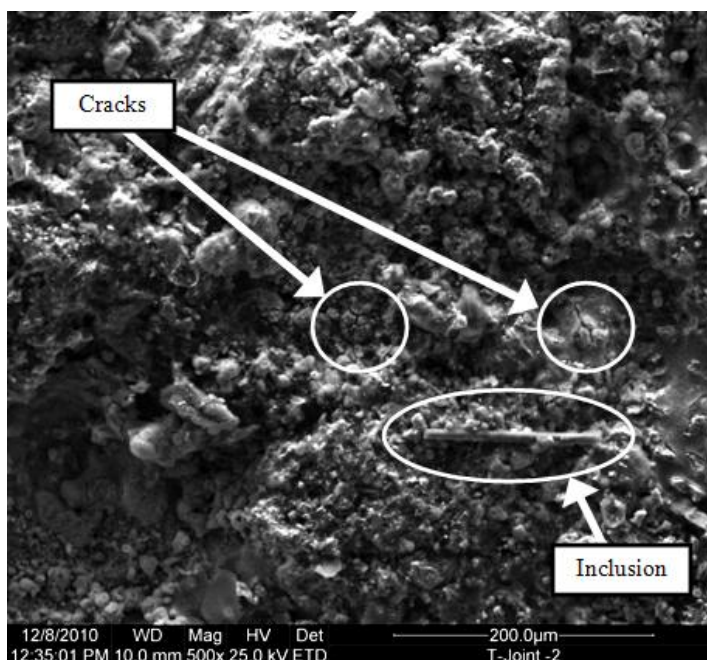

Figure 24. The EDS spectrum of the second location

**Figure 25.** The SEM image at the first location at 500X showning deposits and cracks

Figure 26. The SEM image of the second location at 500X showning cracks and an inclusion

Noting that water is usually used in heat exchangers or in electric generators in oil and gas plants strengthen this statement. The locations of interest were examined under the scanning electron microscope and their features were inspected. Cracks and deposits were important features that helped determine the failure mechanism and working fluid.

3.9. Simulation

Flow simulation is carried out using SolidWorks [24]. Flow Simulation on undamaged and damaged (i.e. eroded) models with the boundary conditions shown in Figure 27. Using flow simulation results (Figure 28), fatigue analysis is performed assuming repeated loading conditions. The results include cut plots of the velocity contours and vectors, the turbulence intensity contours, the velocity contours and vectors of the eroded section, the pressure contours of the eroded section, the fatigue load factor of the eroded section. From these figures, it is noted that the flow from the 2 m/s velocity inlet directly hits the eroded location and that a swirl is developed in that location. It can also be seen that the highest turbulence intensity is noted in the eroded location. These observations indicate that our earlier discussion of flow direction is valid. It is also noted that the swirl developed is growing in size as the location erodes. The highest pressure is noted in the vicinity of the eroded location. This indicates that the eroded location is under high loads. It can also be noted that the eroded location is susceptible to fatigue. Noting that this location has a very rough surface and thin walls, and that fatigue life is highly depended on surface condition, the eroded location is, in fact, the location most susceptible to fatigue cracking. FEA greatly helped in determining and verifying the failure mechanism.
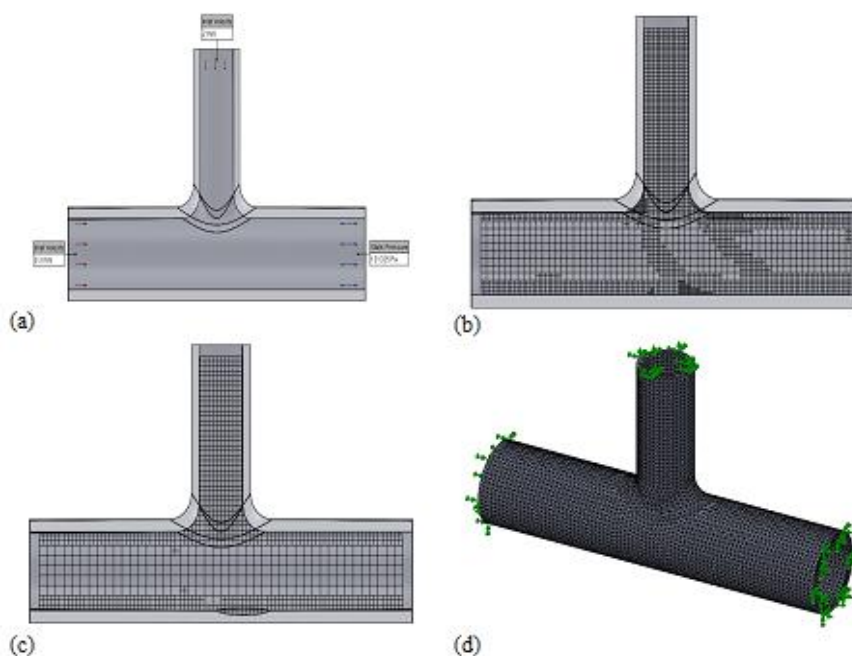

Figure 27. (a): Section of the T-joint model with boundary condition (b) The mesh of undamaged T-joint model (c) The mesh of the eroded T-joint model (d) Complte model.

The failure mechanism includes the combined effect of erosion, corrosion and fatigue. The failure mechanism is believed to be as follows:
- Fast flowing fluid continuously eroded the surface.
- Corrosion has occurred throughout the lifetime of the component.

- The combined effect of erosion and corrosion accelerated material removal in the location under the most sever conditions.
- Pits formed on the rough eroded surface where water stagnates during shutdowns.
- Pressure variations initiated small cracks on the rough eroded inner surface of the T-joint, or the cracks initiated from one of the pits.
- As pressure fluctuated inside the T-joint, the cracks in the weakest location started to grow till it reached the outer surface.

A leakage was noted on the outer surface.
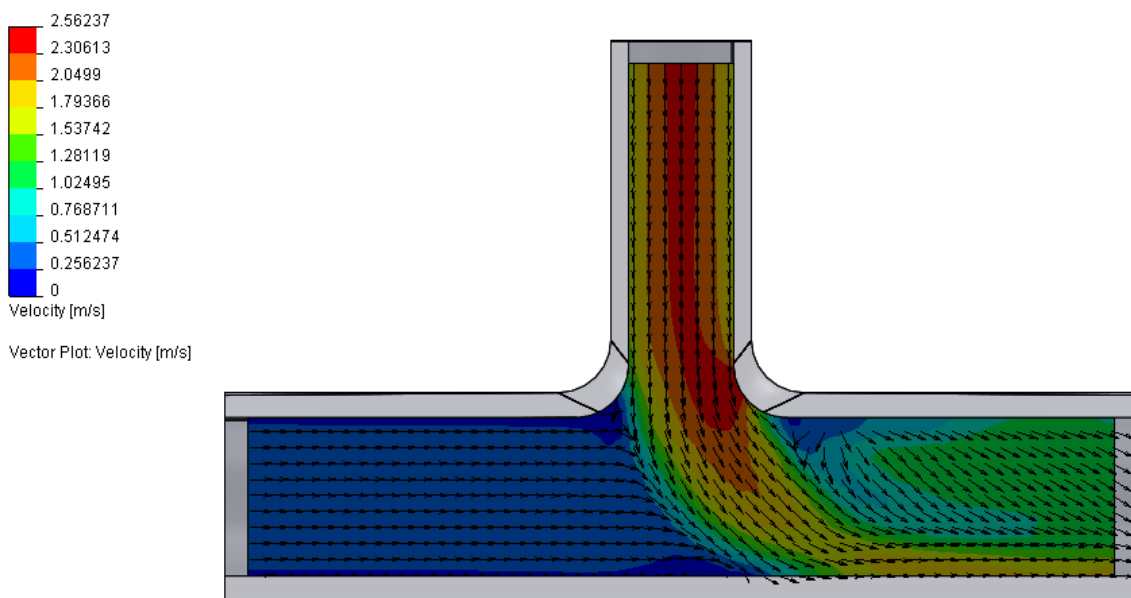
Figure 28a. A cut plot of the velocity contours and vectors of the T-joint model
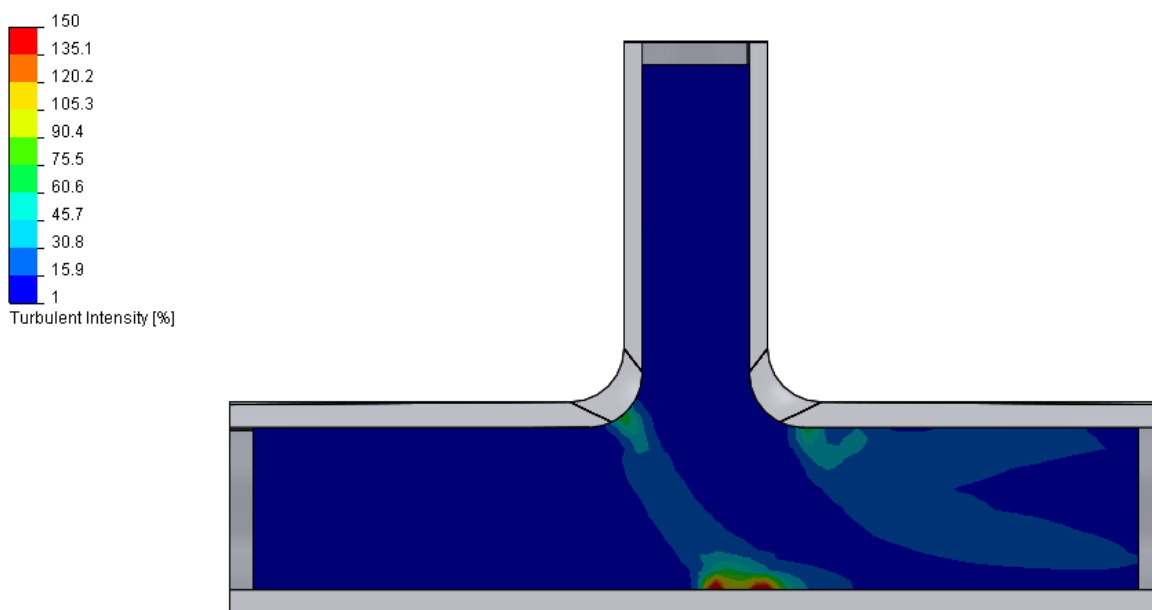
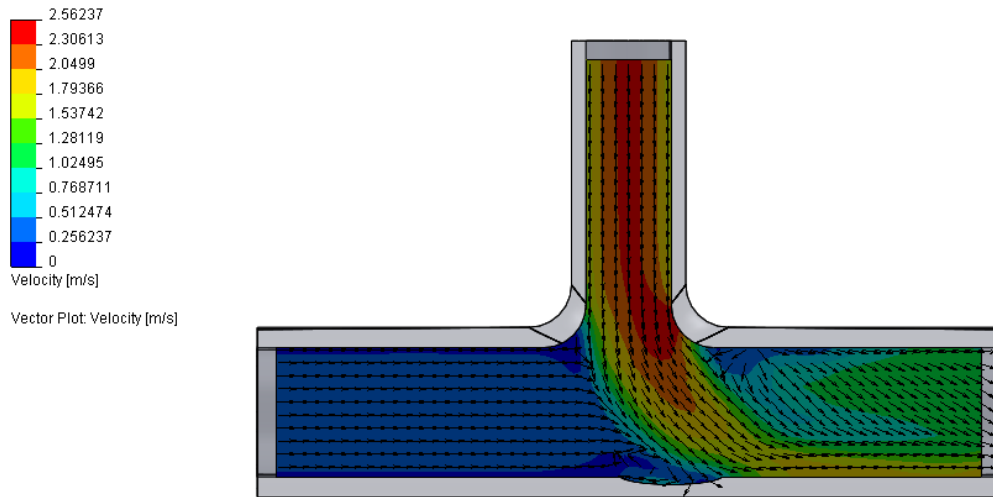**Figure 28b.** A cut plot of the turbulence intensity contours of the T-joint model

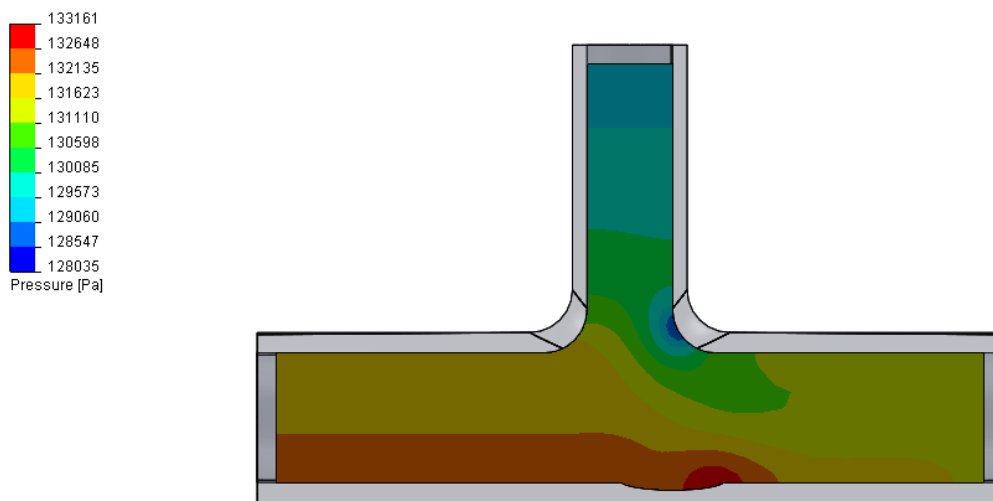**Figure 28c**. A cut plot of the velocity contours and vectors of the eroded T-joint model

Figure 28d. A cut plot of the pressure contours of the eroded T-joint model
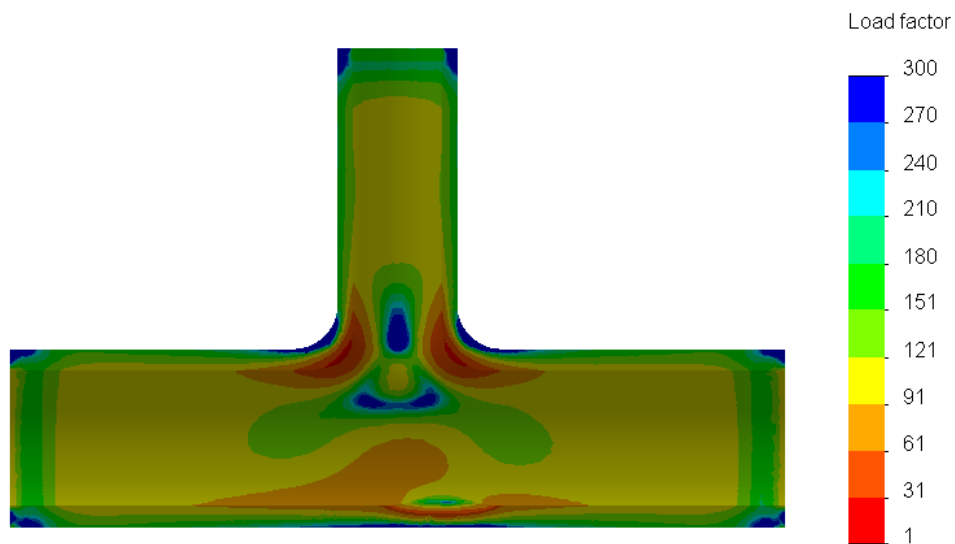

Figure 28e. A section plot of the fatigue load factor of the eroded T-joint model

5. CONCLUSIONS

The material of the T-joint is Low Carbon Steel (AISI 1026). Inclusions are noted in the material. The harsh working conditions are believed to have caused the failure. The failure is believed to have started with erosion which reduced the thickness of the wall at the location of leakage. General corrosion and pitting are believed to have helped in initiating a crack which ultimately led to leakage when it reached the outer surface of the T-joint. The crack grew due to the fluctuation of the pressure inside the T-joint. Using a Y-joint is believed to be one of the possible solutions for this failure.

References

1. R. Réquiz, S. Camero, A. L. Rivas, *Microsc Microanal* 11 (2005) 1992.
2. F. Mohammadi, J. Luo, *Corros. Sci.* 52 (2010) 2994.
3. R.J.K. Wood, Wear 261, 1012 (2006).
4. A.W. Hassel, A.J. Smith, *Corros. Sci.* 49 (2007) 231.
5. G.T. Burstein, K. Sasaki, *Electrochim. Acta* 46 (2001) 3675.
6. K. Sasaki, G.T. Burstein, *Corros. Sci*. 49 (2007) 92.
7. A.J. Smitha, M. Stratmann, A.W. Hassel, *Electrochim. Acta* 51 (2006) 6521.
8. ASM handbook, Vol. 11, "Failure Analysis and Prevention" ASM International Handbook Committee, Materials Park, Ohio: ASM International, 2002.
9. J.R. Still, P. Nelson, Materials & Design 10 (1989) 307
10. K. N. Cho, W.I. Ha, C.D. Jang, S.J. Kang, Marine Structures 4 (1991)57
11. A.J McEvily, Engineering Failure Analysis 11 (2004) 167
12. J. Ahmad, J. Purbolaksono, L.C. Beng, A.Z. Rashid, A. Khinani, A.A. Ali, Engineering Failure Analysis, 16 (2009) 2325
13. Y. Yin, Q.H. Han, L.J. Bai, H.D. Yang, S.P. Wang. Journal of Constructional Steel Research, 65 (2009) 326
14. M. M. K. Lee. Journal of Constructional Steel Research, 51 (1999) 265
15. Chi King Lee, Lie Seng Tjhen, Chiew Sing Ping, Shao Yongbo. Engineering Fracture Mechanics, 72 (2005) 983
16. B. Wang, N. Hu, Y. Kurobane, Y. Makino, S. T. Lie. Engineering Structures, 22 (2000) 424
17. X. Wang, S.B. Lambert, International Journal of Fatigue, 25 (2003)89.
18. A. Rauf, E. Mahdi, *Journal of New Materials for Electrochemical Systems* 15 (2012) 107.
19. K. Yamakawa, H. Inoue, *Corros. Sci.* 31 (1990) 503.
20. M. Hashimoto, S. Miyajima, T. Murata, *Corros. Sci*. 33 (1992) 885.
21. L. Vrsalović, M. Kliškić, J. Radošević, S. Gudić, *J. Appl. Electrochem.* 35 (2005) 1059.
22. G.A. Zhang, Y.F. Cheng, *Corros. Sci*. 51 (2009) 901.
23. http://www.ejsong.com/mdme/memmods/MEM30007A/steel/steel.html
24. SolidWorks, User's Manual, theory manual, version 10. Dassault Systèmes SolidWorks Corp.